We are IntechOpen, the world's leading publisher of Open Access books
Built by scientists, for scientists

6,900
Open access books available

185,000
International authors and editors

200M
Downloads

Our authors are among the

154
Countries delivered to

TOP 1%
most cited scientists

12.2%
Contributors from top 500 universities

WEB OF SCIENCE™

Selection of our books indexed in the Book Citation Index in Web of Science™ Core Collection (BKCI)

Interested in publishing with us?
Contact book.department@intechopen.com

Numbers displayed above are based on latest data collected.
For more information visit www.intechopen.com

Chapter 6

Photoionization Cross Section in Low-Dimensional Systems

Moletlanyi Tshipa and Monkami Masale

Additional information is available at the end of the chapter

http://dx.doi.org/10.5772/intechopen.75736

Abstract

A theoretical investigation of the effects of the parabolic, shifted parabolic, hill-like, and cup-like parabolic confining electric potentials on photoionization cross section (PCS) in a spherical quantum dot is presented. Each of the parabolic potentials is superimposed on an infinite spherical square quantum well (ISSQW) potential. The parabolic potential blueshifts the peaks of the PCS, while the shifted parabolic potential causes a redshift. As the so-called strength of cup-like parabolic potential is increased, the peak of the PCS becomes redshifted for the $s \rightarrow p$ transition, but blueshifted for the $p \rightarrow d$, $d \rightarrow f$ (and so forth) transitions. On the contrary, an increase in the strength of the hill-like parabolic potential blueshifts peaks of the PCS for $s \rightarrow p$ transitions, while it redshifts those of transitions between higher states.

Keywords: photoionization cross section, confining electric potential, spherical quantum dot, hydrogenic impurity

1. Introduction

Recent advances in nanofabrication technology have made it possible to fabricate nanostructures of different sizes and geometries [1–3]. Nanostructures have a wide range of applications including in nanomedicine [4, 5], optoelectronics [6, 7], energy physics [8–12], and gas sensing [13]. Now, even with utmost care and employing the most advanced techniques, it is not possible to fabricate nanostructures which are free of impurities. It may be advantageous, however, to introduce impurities into a nanostructure at the fabrication stage. The presence of such deliberately introduced impurities can lead to improved performance of nanodevices, for example, enhancement of electrical conductivity of semiconducting materials [14]. The impurity may actually be positively charged, in which case an electron may become

IntechOpen

© 2018 The Author(s). Licensee IntechOpen. This chapter is distributed under the terms of the Creative Commons Attribution License (http://creativecommons.org/licenses/by/3.0), which permits unrestricted use, distribution, and reproduction in any medium, provided the original work is properly cited. CC BY

bound to it, thus forming an electron-hole pair. Photoionization is one of the useful probes for the particular nature of electron-impurity interactions in low-dimensional systems. In the process of photoionization, upon absorbing sufficiently enough energy from the irradiating electromagnetic field, the electron can break free from the impurity. In a sense, photoionization is the classical analog of the binding energy problem. Certainly, the subtlety in photoionization effects is in the variety of conditions in low-dimensional systems. These conditions include quantization of the electron's energy levels as well as the optical properties of the specimen.

In this regard, photoionization studies on nanostructures could offer insight into the electron-impurity interaction in a wide variety of conditions. These photoionization effects have fueled significant interest in the processes of photoionization in low-dimensional systems. The effects of geometry and hydrostatic pressure on photoionization cross section (PCS) have been reported in concentric double quantum rings [15]. The effect of applied electric field on photoionization cross section has also been probed in cone-like quantum dots [16]. The role that impurity position plays in modifying the PCS in a core/shell/shell quantum nanolayer [17] and a purely spherical quantum has been investigated [18]. Overall, it has been found that photoionization transitions are independent of the photon polarization for a centered impurity, while the transitions are dependent on the photon polarization when the impurity is off-centered. Influences of intense laser field and hydrostatic on PCS in pyramid-shaped quantum dots have also been reported [19]. There also have been studies of PCS in spherical core/shell zinc blende quantum structures under hydrostatic pressure and electric field [20].

In this chapter, the effect of geometry of confining electric potential on centered donor-related PCS in spherical quantum dots is investigated. The electric potentials considered are the parabolic, shifted parabolic, cup-like, and the hill-like potentials, all of which have a parabolic dependence on the radial distance of the spherical quantum dot. To start with, the Schrödinger equation is solved for the electron's eigenfunctions and energy eigenvalues within the effective mass approximation. It is emphasized that the treatment of photoionization process given here is limited only to isotropic media.

2. Theory

The basic problem of photoionization involves an electron deemed to be bound to a donor charge or indeed a center of positive charge embedded in a semiconductor specimen. An electron, upon absorbing sufficiently enough energy from the irradiating electromagnetic field, can be "liberated" from the electrostatic field of the positive charge. Now, in low-dimensional systems, the energy of an electron is quantized into different energy levels. The process of photoionization can thus involve intermediate transitions wherein an electron in some initial state $|i\rangle$ absorbs a photon of energy $\hbar\omega$ and thereby makes a transition to a final state $|f\rangle$. It is worth noting that in photoionization calculations, the initial states of the electron are described by wave functions taking into account the presence of the impurity. The final states, however, are described by the wave functions in the absence of the impurity. This notion of taking the initial and final quantum states of the electron, in a sense, is a simulation of calculations of the

binding energies in classical mechanics. The energies of the corresponding initial and final states are E_i and E_f, respectively. The system investigated here is a spherical quantum dot (SQD) of refractive index n and relative dielectric constant ε, which may be a GaAs material embedded in a $Ga_{1-x}Al_xAs$ matrix, with a donor impurity embedded at its center. Now, one of the physical quantities that are useful in the description of this binding energy-like problem is called photoionization cross section. This quantity may be regarded as the probability that a bound electron can be liberated by some appropriate radiation per unit time per unit area, given by [15–20]

$$\sigma_{lm} = \sigma_o \hbar\omega \sum_f \left| \left\langle f \right| \vec{r} \left| i \right\rangle \right|^2 \delta\left(E_f - E_i - \hbar\omega\right) \tag{1}$$

where $\left| \left\langle f \right| \vec{r} \left| i \right\rangle \right|$ is the interaction integral coupling initial states to final states, α_{FS} is the fine structure constant and $\vec{r}$ is the electron position vector. Finally, the amplitude of the PCS is given by $\sigma_o = 4\pi^2 \alpha_{FS} n E_{in}^2 / \left(3E_{av}^2 \varepsilon\right)$ in which E_{in} is the effective incident electric field and E_{av} the average electric field inside the quantum dot. Evaluation of the matrix elements for an SQD leads to the selection rules $\Delta l = \pm 1$ [21], that is, the allowed transitions are only those for which the l values of the final and initial states will be unity. In the investigations carried out here, the evaluations of the PCS are for transitions only between two electron's energy subbands. For purposes of computation, therefore, the Dirac delta function in Eq. (1) is replaced by its Lorentzian equivalent given by

$$\delta\left(E_f - E_i - \hbar\omega\right) = \frac{\hbar\Gamma}{\left(E_f - E_i - \hbar\omega\right)^2 + \left(\hbar\Gamma\right)^2}, \tag{2}$$

where this is the so-called Lorentzian linewidth.

Now, in view of spherical symmetry, the solutions of the Schrödinger wave equation are sought in the general form $\Psi_{lm}(r,\theta,\varphi) = C_{lm} Y_{lm}(\theta,\varphi)\chi(r)$, where C_{lm} the normalization constant, $Y_{lm}(\theta,\varphi)$ the spherical harmonics of orbital momentum and magnetic quantum numbers l and m, respectively. The radial part of the total wave function, $\chi(\rho)$, is found to be the following linear second-order differential equation

$$\frac{1}{r^2}\frac{d}{dr}\left(r^2 \frac{d\chi(r)}{dr}\right) + \left\{\frac{2\mu}{\hbar^2}\left[E_{lm} + \frac{k_e e^2}{\varepsilon r} - V(r)\right] - \frac{l(l+1)}{r^2}\right\}\chi(r) = 0 \tag{3}$$

where μ is the effective mass of electron (of charge -e) and k_e is the Coulomb constant.

2.1. The electron's wave functions

The specific forms of the solutions of the differential equation described above depend on the particular electric confining potential considered. Here, the different radially dependent forms of the so-called intrinsic electric confinement potential of the spherical quantum dot, in turn, taken into account in solving Eq. (3) are (shown in **Figure 1**) (1) simple parabolic, (2) shifted

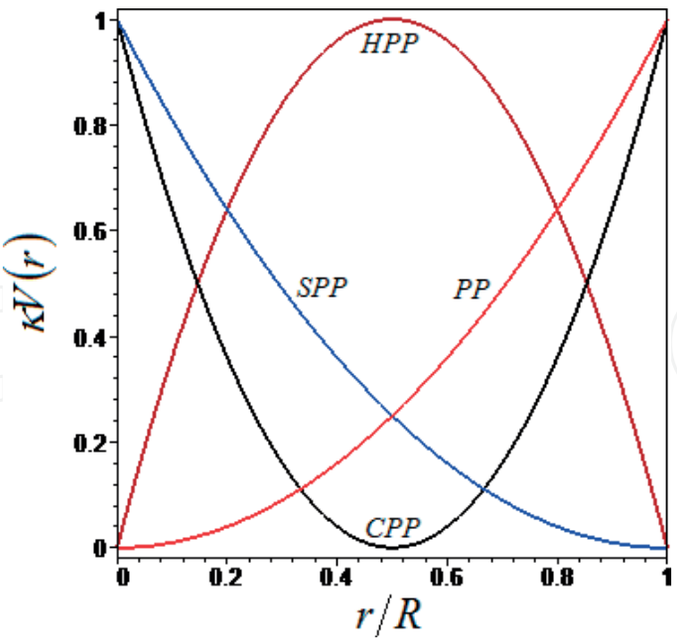

Figure 1. The spatial variation of the confining electric potentials across the SQD: simple parabolic potential (PP), shifted parabolic potential (SPP), cup-like potential (CPP), and the hill-like potential (HPP).

parabolic, (3) bi-parabolic (cup-like), and (4) inverse bi-parabolic (hill-like), each superimposed on an infinite spherical square quantum well (ISSQW).

2.1.1. Parabolic potential

When the parabolic potential (PP), which has the form

$$V(r) = \frac{1}{2}\mu\omega_0^2 r^2, \qquad (r < R) \tag{4}$$

and infinity elsewhere, is inserted into the Schrödinger equation (Eq. (2)) in the presence of the donor impurity, then the second-order differential equation is solvable in terms of the Heun biconfluent function [22, 23].

$$\chi(\rho) = C_{1lm} e^{g_1(r)} r^l HeunB\big(2l+1, \alpha, \beta, \gamma, g_2(r)\big) + C_{2lm} e^{g_1(r)} r^{-(l+1)} HeunB\big(-(2l+1), \alpha, \beta, \gamma, g_2(r)\big) \tag{5}$$

with

$$\alpha = 0, \quad \beta = -\frac{2E_{lm}}{\hbar\omega_0}, \gamma = \frac{4k_e e^2}{\varepsilon\hbar}\sqrt{-\frac{\mu}{\hbar\omega_0}} \tag{6}$$

and the arguments

http://dx.doi.org/10.5772/intechopen.75736

$$g_1(r) = \frac{\mu\omega_0}{2\hbar} r^2, \text{ and } g_2(r) = \sqrt{2g_1(r)}. \tag{7}$$

Eq. (5) is the complete solution of the differential equation given earlier; however, the second solution diverges at the origin and so C_{2lm} must be taken as zero. The application of the standard boundary condition of continuity of the wave function at the walls ($r = R$) of the SQD leads to the following electron's energy eigenvalue equation:

$$HeunB\big(2l+1, \alpha, \beta_E, \gamma, g_2(R)\big) = 0. \tag{8}$$

The electron's energy spectrum is derived from numerically solving Eq. (8) for its roots β_E according to

$$E_{lm} = -\frac{\beta_E}{2}\hbar\omega_0. \tag{9}$$

2.1.2. Shifted parabolic potential

This potential is convex: maximum at the center and decreases parabolically to assume a minimum value (here taken as zero) at the radius

$$V(r) = \frac{1}{2}\mu\omega_o^2(r-R)^2, \qquad (r < R) \tag{10}$$

and infinity elsewhere. The solution to the radial component of the Schrödinger equation (Eq. (3)) corresponding to this potential is also in terms of the Heun biconfluent function (Eq. (5)) but with [23]

$$\alpha = 2\sqrt{-\frac{\mu\omega_0 R^2}{\hbar}}, \quad \beta = -\frac{2E_{lm}}{\hbar\omega_0}, \gamma = \frac{4k_e e^2}{\varepsilon\hbar}\sqrt{-\frac{\mu}{\hbar\omega_0}} \tag{11}$$

and the arguments

$$g_1(r) = \frac{\mu\omega_0}{2\hbar}(r-2R)r \text{ and } g_2(r) = -i\sqrt{\frac{\mu\omega_0}{\hbar}}r \tag{12}$$

The energy spectrum is given by the usual boundary conditions at the walls of the SQD as

$$E_{lm} = -\frac{\beta_E}{2}\hbar\omega_0 \tag{13}$$

where β_E is the value of β that satisfies the condition given in Eq. (8).

2.1.3. The bi-parabolic (cup-like) potential

The solution to the Schrödinger equation for the bi-parabolic potential

$$V(r) = \frac{1}{2}\mu\omega_0^2(r - R/2)^2, \tag{14}$$

and infinity elsewhere, in the presence of the impurity, is in terms of the Heun biconfluent function (Eq. (5)) [24] with

$$\alpha = iR\sqrt{\frac{\mu\omega_0}{\hbar}}, \beta = -\frac{2E_{lm}}{\hbar\omega_0}, \gamma = -\frac{4ik_e e^2}{\varepsilon\hbar}\sqrt{\frac{\mu}{\hbar\omega_0}} \tag{15}$$

and the arguments

$$g_1(\rho) = \frac{\mu\omega_0}{2\hbar}(\rho - R)\rho, \text{ and } g_2(\rho) = -i\sqrt{\frac{\mu\omega_0}{\hbar}}\rho. \tag{16}$$

Requiring that the electron wave function should vanish at the walls of the SQD avails the energy spectrum for an electron in an SQD with an intrinsic bi-parabolic potential as

$$E_{lm} = -\frac{\beta_E}{2}\hbar\omega_0 \tag{17}$$

where β_E is the value of β that satisfies the condition stipulated in Eq. (8).

2.1.4. The inverse lateral bi-parabolic (hill-like) potential

The hill-like potential has a concave parabolic increase in the radial distance from the center to reach maximum at a radial distance half the radius $(r = R/2)$, after which a concave parabolic decrease brings it to a minimum at the walls of the SQD $(r = R)$

$$V(r) = \frac{1}{2}\mu\omega_o^2\left(Rr - r^2\right), \qquad (r < R) \tag{18}$$

and infinity elsewhere. The radial component of the Schrödinger equation for this potential in the presence of the impurity is also solvable in terms of the Heun biconfluent function (Eq. (5)) but with [24]

$$\alpha = R\sqrt{\frac{\mu\omega_0}{i\hbar}}, \beta = \frac{\left(\mu\omega_0^2R^2 - 8E_{lm}\right)}{4i\hbar\omega_0}, \gamma = -\frac{4ik_e e^2}{\varepsilon\hbar}\sqrt{\frac{-\mu}{i\hbar\omega_0}} \tag{19}$$

and the arguments

$$g_1(r) = \frac{\mu\omega_0}{2i\hbar}(R\text{-}r)r \text{ and } g_2(r) = \sqrt{\frac{-i\mu\omega_0}{\hbar}}r. \tag{20}$$

Application of the boundary conditions at the walls of the SQD avails the energy spectrum as

$$E_{lm} = \frac{1}{8}\mu\omega_0^2R^2 - \frac{i\beta_E}{2}\hbar\omega_0 \tag{21}$$

with β_E being the value of β that satisfies the condition set in Eq. (8).

3. Results and discussions

The parameters used in these calculations are relevant to *GaAs* quantum dots: effective electronic mass $\mu = 0.067m_e$, m_e being the free electron mass and $\varepsilon = 12.5$. The impurity linewidth has been taken such that $\hbar\Gamma = 0.1\ meV$ [18, 19]. The spatial variation of the confining electric potentials across the SQD is illustrated in **Figure 1**, where $\kappa = \left[2/\left(\mu\omega_0^2R^2\right)\right]$. **Figure 2** displays the effects of these potential geometries on the ground-state radial electron wave functions across an SQD of radius $R = 250$ Å in the absence of the hydrogenic impurity. The parabolic potential shifts the electron wave functions toward the center of the SQD, while the shifted parabolic potential (SPP) shifts the electron wave functions toward the walls of the SQD. As stated earlier, the cup-like is zero at $r = 0.5R$ but maximum at both the center and at the walls of the SQD. Thus, this potential tends to "concentrate" the electron's wave functions of the excited states to regions near $r = 0.5R$ but diminish the ground-state wave functions near regions where it is maximum. By contrast, the hill-like potential is maximum at $r = 0.5R$ and thus has the opposite effect on the respective electron's wave functions.

Figure 3 depicts the variation of the first-order $(s \rightarrow p)$ and second-order $(p \rightarrow d)$ transition energies as functions of the strengths of the potentials, viz: the parabolic potential (PP), shifted parabolic potential (SPP), the cup-like potential (CPP), and the hill-like potential (HPP). These are the differences in the energies of states between which an electron is allowed to make transitions within the dipole approximation during photoionization. Now, in the absence of the impurity, the first-order transition energies ΔE_{sp} are always lower than those of second-order transition ΔE_{pd}, that is, for all values of nano-dot radius. In the presence of the impurity, however, there is some characteristic radius R_0 at which the first-order and the second-order

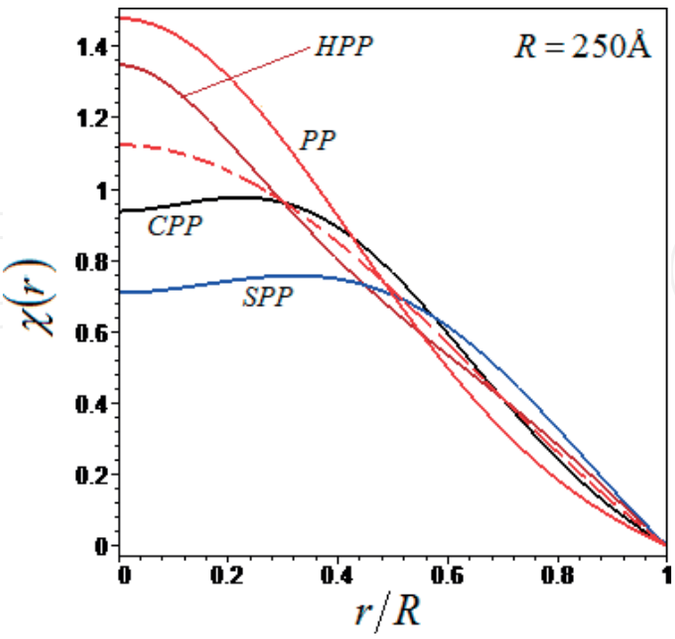

Figure 2. The effect of the different potentials on the ground-state radial electron wave function for an SQD of radius $R = 250$ Å. The potentials, parabolic (PP), shifted parabolic (SPP), cup-like (CPP), and the hill-like (HPP) all have strength $\hbar\omega_0 = 10$ meV. The dashed curve represents ground-state electron wave function in an ISSQW ($\hbar\omega_0 = 0$ meV).

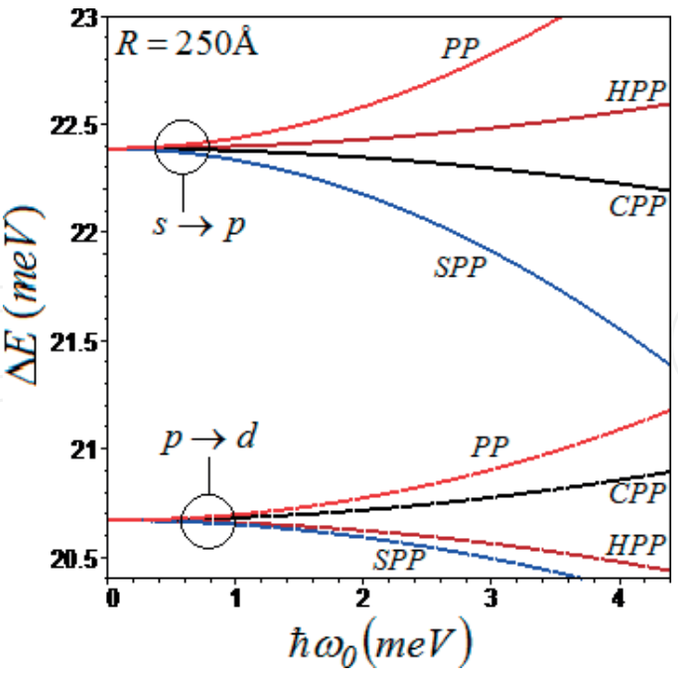

Figure 3. The dependence of the first- $(s \rightarrow p)$ and second $(p \rightarrow d)$-order transition energies on the strengths of the different potentials, viz.: the parabolic potential (PP), shifted parabolic potential (SPP), the cup-like potential (CPP), and the hill-like potential (HPP), for an SQD of radius R = 250 Å.

transition energies coincide. For the system investigated here, this radius is in the neighborhood of $R_0 = 171$ Å. For SQDs with radii less (greater) than R_0, the second-order transition energies are more (less) than the first-order transition energies. The parabolic potential and hill-like potentials reduce the value of this radius as they intensify. On the contrary, increasing the strengths of the shifted parabolic potential and the cup-like potentials increases R_0, sending it to infinity as it intensifies further. In this case, ΔE_{sp} and ΔE_{pd} would never coincide and $\Delta E_{pd} > \Delta E_{sp}$. The parabolic potential widens the gap between the energies of the initial and final states, regardless of the order of transition. The increase is more pronounced in transitions involving the lower states than in transitions involving the higher states. The shifted parabolic potential decreases transition energies also regardless of the order of transition, and with the reduction being more pronounced for transitions involving the lower states than in those involving the higher states. However, the situation is not so straightforward with the cup-like and the hill-like potentials. The cup-like potential decreases transition energies of only transitions involving the ground (s) state and enhances transition energies involving higher states. The hill-like potential increases only the transition energies involving the ground state but decreases transition energies involving higher states.

Figure 4 shows the sum of the $s \rightarrow p$ and $p \rightarrow d$ normalized photoionization cross sections for an SQD of radius $R = 250$ Å, where the dashed curve is for an ISSQW ($\hbar\omega_0 = 0$ meV) while the solid curve corresponds to the parabolic potential of strength $\hbar\omega_0 = 5$ meV superimposed on the ISSQW. Here, as in subsequent figures, the radius of the SQD is greater than R_0, thus the $s \rightarrow p$ peak occurs at larger beam energies than the second-order peak. Increasing the strength

http://dx.doi.org/10.5772/intechopen.75736

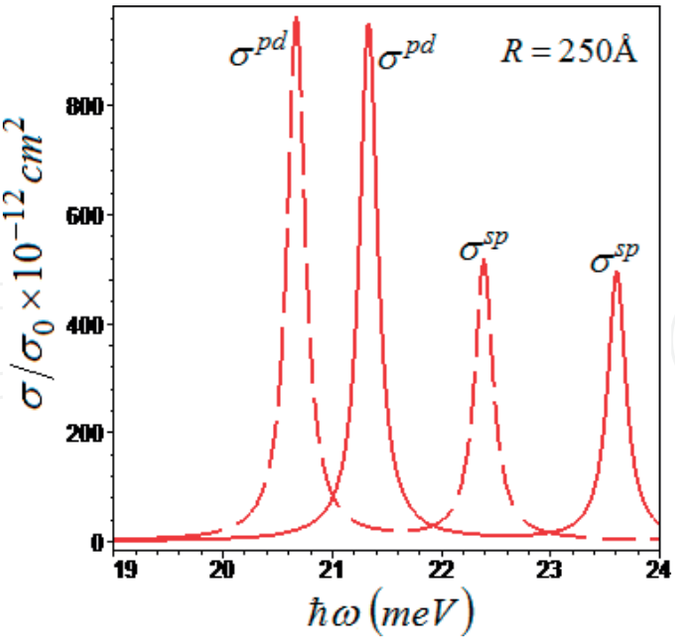

Figure 4. The sum of the first- and second-order normalized PCSs as functions of beam energy for the ISSQW (dashed curves) and for an SQD with the parabolic potential of strength $\hbar\omega_0 = 5$ meV superimposed on an ISSQW (solid plots), for a radius $R = 250$ Å.

of the parabolic potential blueshifts the peaks of the PCS, simultaneously moving them apart. This can be beneficial in cases where transitions between different states (e.g., the $s \rightarrow p$ and the $p \rightarrow d$ transitions) need to be isolated and distinct, for research or practical purposes.

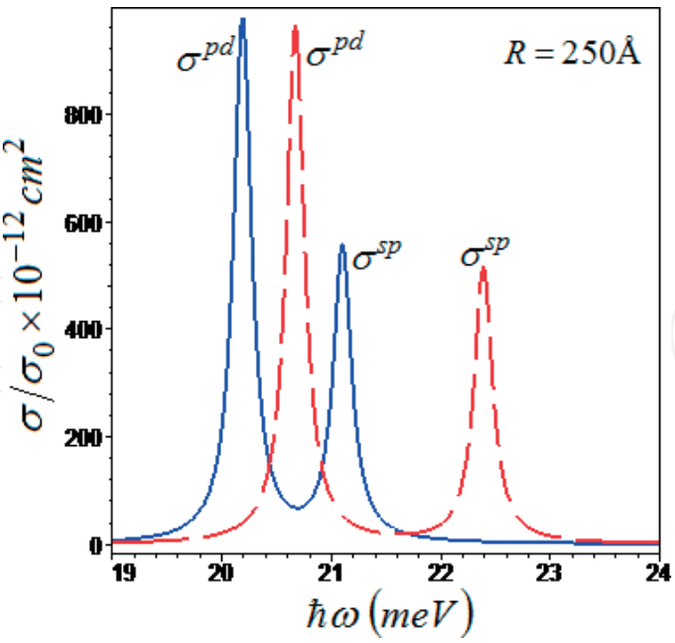

Figure 5. The sum of the first- and second-order normalized PCSs as functions of beam energy for the ISSQW (dashed curves) and for an SQD with the shifted parabolic potential of strength $\hbar\omega_0 = 5$ meV superimposed on an ISSQW, for a radius $R = 250$ Å.

Figure 5 depicts the summed normalized PCS for the $s \rightarrow p$ and $p \rightarrow d$ transitions in an SQD of radius $R = 250$ Å. The dashed curve is associated with the ISSQW ($\hbar\omega_0 = 0$ meV) while the solid plot corresponds to PCS for an SQD with a shifted parabolic potential of the so-called strength such that $\hbar\omega_0 = 5$ meV. Overall, the shifted parabolic potential redshifts the resonance peaks of the PCSs. It is interesting to note, however, that the first-order resonance peak redshifted to a much greater extent than that of the second order. These results suggest that the shifted parabolic potential can be utilized to manipulate the first-order and second-order transitions according to their corresponding photon energy of excitation [23].

Figure 6 illustrates the normalized $s \rightarrow p$ and $p \rightarrow d$ PCSs as functions of the photon energy for an SQD of radius $R = 250$ Å. The dashed curve is for the purely ISSQW ($\hbar\omega_0 = 0$ meV) while the solid plot is for the cup-like potential of strength $\hbar\omega_0 = 5$ meV superimposed on the ISSQW. As can be clearly seen from the figure, the cup-like potential redshifts peaks of the $s \rightarrow p$ PCS while it blueshifts the peaks of the $p \rightarrow d$ PCS. This potential also blueshifts peaks of PCS of transitions involving higher states ($d \rightarrow f, f \rightarrow g$ and so forth).

Figure 7 depicts the variation of the normalized $s \rightarrow p$ and $p \rightarrow d$ PCSs with the photon energy for an SQD of radius $R = 250$ Å. Here also, the dashed curve represents the purely ISSQW ($\hbar\omega_0 = 0$ meV) while the solid plot is for the hill-like potential of strength $\hbar\omega_0 = 5$ meV superimposed on the ISSQW. Increasing the strength of the hill-like potential blueshifts the peaks of the $s \rightarrow p$ PCS while it redshifts those of the $p \rightarrow d$ PCS. Although not shown here, the hill-like potential also redshifts peaks of the PCS associated with transitions from higher states ($d \rightarrow f, f \rightarrow g$ and so forth).

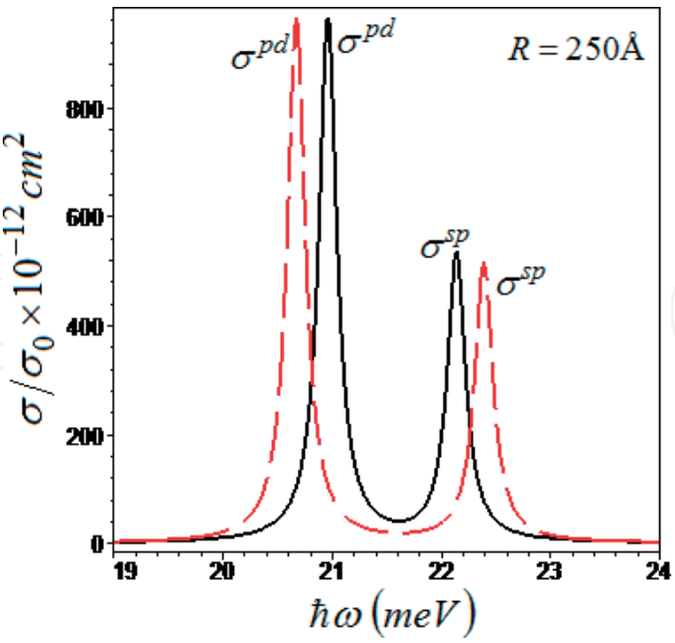

Figure 6. The sum of the first- and second-order normalized PCSs as functions of beam energy for the ISSQW (dashed curves) and for an SQD with the cup-like potential of strength $\hbar\omega_0 = 5$ meV superimposed on an ISSQW, for a radius $R = 250$ Å.

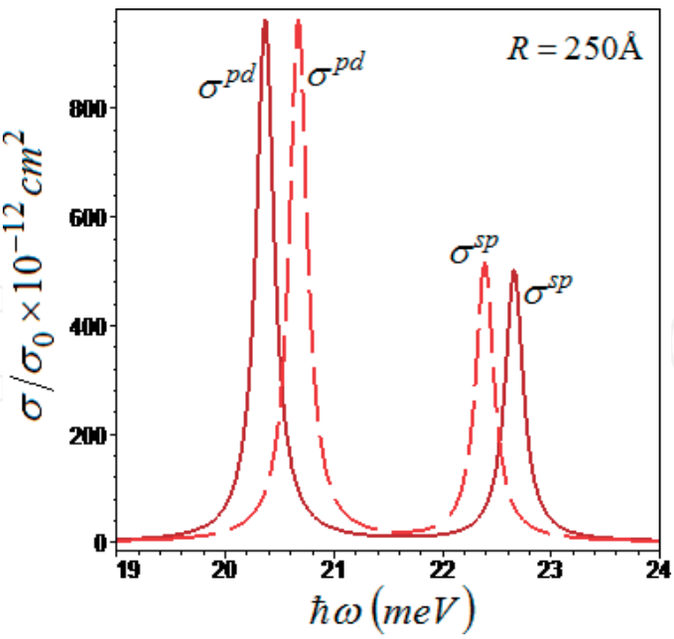

Figure 7. The sum of the first- and second-order normalized PCSs as functions of beam energy for the ISSQW (dashed curves in both) and for an SQD with the hill-like potential of strength $\hbar\omega_0 = 5$ meV superimposed on an ISSQW, for a radius $R = 250$ Å.

4. Conclusions

The electron's wave functions in a spherical quantum dot with a centered donor impurity have been obtained, and these were utilized to evaluate the effects of the geometry of confining electric potentials on PCS in an SQD. The parabolic potential enhances photoionization transition energies independent of the initial or the final state, while the shifted parabolic potential decreases the transition energies, also independent of the order of transition. As a result, the parabolic potential blueshifts the peaks of the PCS, while the shifted parabolic potential redshifts the peaks, for all transitions. The cup-like and the hill-like potentials exhibit a selective enhancement or a reduction of transition energies. The hill-like parabolic potential enhances the transition energies involving the ground state but dwindles those involving higher states. A consequence of this effect is that the hill-like parabolic potential blueshifts peaks of $s \rightarrow p$ PCS but redshifts those involving higher states. The situation is the other way around in the case of the cup-like parabolic potential. The results presented here also suggest that nano-patterning techniques may offer yet another method of tuning the process of photoionization to resonance, through tailored electric potentials.

Conflict of interest

The authors have no conflict of interest to declare.

Author details

Moletlanyi Tshipa* and Monkami Masale

*Address all correspondence to: tshipam@mopipi.ub.bw

University of Botswana, Gaborone, Botswana

References

[1] Meng L, He X, Gao J, Li J, Wei Y, Yan J. A novel nanofabrication technique of silicon-based nanostructures. Nanoscale Research Letters. 2016;**11**:504. DOI: 10.1186/s11671-016-1702-4

[2] Moura I, de Sá A, Abreu AS, Oliveira M, Machado AV. Morphology, optical, and electric properties of polymer-quantum dots nanocomposites: Effect of polymeric matrix. Journal of Materials Science. 2016;**51**:8699-8710. DOI: 10.1007/s10853-016-0129-8

[3] Sadeghimakki B, Zheng Y, Jahed NMS, Sivoththaman S. Synthesis of CIS quantum dots in low-temperature regime: Effects of precursor composition and temperature ramps. IEEE Transactions on Nanotechnonlogy. 2017;**16**(4):659-666. DOI: 10.1109/TNANO.2017.2703162

[4] Chan WCW, Maxwell DJ, Gao X, Bailey RE, Han M, Nie S. Luminescent quantum dots for multiplexed biological detection and imaging. Current Opinion in Biotechnology. 2002;**13**:40-46

[5] Bwatanglang IB, Mohammad F, Yusof NA, Abdullah J, Hussein MZ, Alitheen NB, Abu N. Folic acid targeted Mn:ZnS quantum dots for theranostic applications of cancer cell imaging and therapy. International Journal of Nanomedicine. 2016;**11**:413-428. DOI: 10.214/IJN.S90198

[6] Chen J, Liu D, Al-Marri M, Nuuttila L, Lehtivuori H, Zheng K. Photo-stability of CsPbBr3 perovskite quantum dots for optoelectronic application. Science China Materials. 2016; **59**(9):719-727. DOI: 10.1007/s40843-016-5123-1

[7] Litvin AP, Martynenko IV, Purcell-Milton F, Baranov AV, Fedorov AV, Gun'ko YK. Colloidal quantum dots for optoelectronics. Journal of Materials Chemisrty A. 2017;**5**: 13252-13275. DOI: 10.1039/c7ta02076g

[8] Li X, Rui M, Song J, Sheh Z, Zeng H. Carbon and grapheme quantum dots for optoelectronic and energy devices: A review. Advanced Materials. 2015;**25**:4929-4947. DOI: 10.1002/adfm.201501250

[9] Lan X, Voznyy O, Kiani A, de Arquer FPG, Abbas AS, Kim G-H, Liu M, Yang Z, Walters G, Xu J, Yuan M, Ning Z, Fan F, Kanjanaboos P, Kramer I, Zhitomirsky D, Lee P, Perelgut A, Hoogland S, Sargent EH. Passivation using molecular halides increases quantum dot solar cell performance. Advanced Materials. 2016;**28**:299-304. DOI: 10.1002/adma.201503657

[10] Xu W-P, Zhang Y-Y, Wang Q, Li Z-J, Nie Y-H. Thermoelectric effects in triple quantum dots coupled to a normal and a superconducting leads. Physics Letters A. 2016;**380**:958-964. DOI: 10.1016/s0014-5793(01)03293-8

[11] Ding W-L, Peng X-L, Sun Z-Z, Li Z-S. Novel bifunctional aromatic linker utilized in CdSe quantum dots-sensitized solar cells: Boosting the open circuit voltage and electron injection. Journal of Materials Chemistry A. 2017;**5**:14319-14330. DOI: 10.1039/c7ta03349d

[12] Cortés N, Rosales L, Chico L, Pacheco M, Orellana PA. Enhancement of thermoelectric efficiency by quantum interference effects in trilayer silicone flakes. Journal of Physics: Condensed Matter. 2017;**29**:015004. DOI: 10.1088/0953-8984/29/1/015004

[13] Yang C, Xiao F, Wang J, Su X. 3D flower- and 2D- sheet-like CuO nanostructures: Microwave assisted synthesis and application in gas sensors. Sensors and Actuators B. 2015;**207**: 177-185. DOI: 10.1016/j.snb.2014.10.063

[14] Xie W. Binding energy of an off-center hydrogenic donor in a spherical Gaussian quantum dot. Physica B: Condensed Matter. 2008;**403**:2828-2831. DOI: 10.1016/j.physb.2008.02.017

[15] Baghramyan HM, Barseghyan MG, Kirakosyan AA, Laroze D, Duque CA. Donor-impurity related photoionization cross section in GaAs/$Ga_{1-x}Al_xAs$ concentric double quantum rings: Effects of geometry and hydrostatic pressure. Physica B: Condensed Matter. 2014;**449**:193-198. DOI: 10.1016/j.physb.2014.05.034

[16] Iqraoun E, Sali A, Rezzouk A, Feddi E, Dujardin F, Mora-Ramos ME, Duque CA. Donor impurity-related photoionization cross section in GaAs cone-like quantum dots under applied electric field. Philosophical Magazine. 2017;**97**(18):1445-1463. DOI: 10.1080/14786435.2017.1302613

[17] Baghdasaryan DA, Kazaryan EM, Sarkisyan HA. Photoionization and electrostatic multipoles properties of spherical core/shell/shell quantum nanolayer with off-center impurity. Superlatticess and Microstructures. 2017;**104**:69-77. DOI: 10.1016/j.spmi.2017.02.017

[18] Ham H, Lee CJ. Photoionization cross section of hydrogenic impurities in spherical quantum dots: Infinite well model. Journal of the Korean Physical Society. 2003;**42**:S688-S692

[19] Niculescu EC. Impurity-related photoionization cross section in a pyramid-shaped quantum dot: Intense laser field and hydrostatic pressure effects. Physica E: Low-dimensional Systems and Nanostructures. 2014;**63**:105-113. DOI: 10.1016/j.physe.2014.05.012

[20] El Ghazi H, Peter AJ. Photoionization cross-section of donor-related in (in,Ga)N/GaN core/shell under hydrostatic pressure and electric field effects. Superlattices and Microstructures. 2017;**104**:222-231. DOI: 10.1016/j.spmi.2017.02.013

[21] Xie W. Hydrostatic pressure effect on photoionization cross section of a Trion in quantum dots. Superlattices and Microstructures. 2013;**63**:10-17. DOI: 10.1016/j.spmi.2013.08.011

[22] Ronveaux A. Heun's Differential Equations. Oxford: Oxford University Press; 1995

[23] Tshipa M. Photoionization cross section in a spherical quantum dot: Effects of some parabolic confining electric potentials. Condensed Matter Physics. 2017;**20**(2):23703:1-9. DOI: 10.5488/CMP.20.23703

[24] Tshipa M. The effects of cup-like and hill-like parabolic confining potentials on photoionization cross section of a donor in a spherical quantum dot. The European Physical Journal B. 2016;**89**:177. DOI: 10.1140/epjb/e2016-60988-6

IntechOpen

IntechOpen